Journal of Metals, Materials and Minerals, 36(3), e2321, 2026

Investigating the effects of $LaMnO_3$ on the morphology, structural and optical properties of epoxy-based plastic scintillators

Yeni FEBRIANTI[1,2], Airine Hijrah HANDAYANI[3], Marzuki NAIBAHO[1], Phahul Zhemas Zul NEHAN[1], ZULKARNAIN[1], Arbi DIMYATI[3], and Budhy KURNIAWAN[1,*]

[1] *Department of Physics, Universitas Indonesia, Depok, West Java, 16424, Indonesia*
[2] *PT Cipta Mikro Material, Kab. Bogor, West Java, 16340, Indonesia*
[3] *Research Center for Nuclear Radiation Detection and Analysis Technology, National Research and Innovation Agency, South Tangerang, 15314, Indonesia*

***Corresponding author e-mail**: budhy.kurniawan@sci.ui.ac.id

Received date:
19 February 2025
Revised date:
25 November 2025
Accepted date:
9 April 2026

Keywords:
$LaMnO_3$;
Plastic scintillator;
Gamma radiation detection

Abstract

Plastic scintillators are widely used in radiation detection due to their low cost, fast response, and ease of fabrication, although their performace is often limited by low density, low atomic number, make them less efficient for applications requiring high-energy radiation. In this study, $LaMnO_3$ was synthesized using the hydrothermal method and employed as a dopant to enhance the optical and scintillation properties of epoxy-based plastic scintillators. Structural, morphological, and optical characterizations of $LaMnO_3$ were carried out using X-ray diffraction (XRD), X-ray photoelectron spectroscopy (XPS), scanning electron microscope (SEM), energy-dispersive spectroscopy (EDS), UV-Vis and photoluminescence (PL) spectroscopy. The results confirm that the synthesized $LaMnO_3$ exhibits a single-phase rhombohedral structure with irragular particle morphology, a direct band gap of 5.48 eV, and broad emission spanning 400 nm to 900 nm. XPS results revealed the coexistence of Mn^{3+} and Mn^{4+} oxidation states, induced by oxygen vacancies in the $LaMnO_3$ lattice. Plastic scintillators were fabricated using epoxy as the matrix, 2,5-Diphenyloxazole (PPO) as the primary scintillator, 1,4-bis(5-phenyloxazol-2-yl)benzene (POPOP) as the wavelength shifter and $LaMnO_3$ as the dopant. UV-Vis and PL measurements show that incorporating $LaMnO_3$, increases optical absorbance, enhances emission intensity, and broadens the emission range, demonstrating more efficient radiative recombination within the scintillator. Pulse-height spectra obtained using photomultiplier tube (PMT) and a ^{60}Co gamma source reveal a clear shift toward higer channels and increase in total counts for the $LaMnO_3$-doped scintillator, confirming improved light output and energy transfer efficiency. Detection efficiency calculations further show that the $LaMnO_3$-doped scintillator achieves 11.59% higher than the 9.86% of the undoped scintillator.

1. Introduction

Research on scintillator materials continues to develop rapidly due to their essential role in converting high-energy radiation, such as X-rays, gamma rays, and charged particles (α and β), into low-energy ultraviolet (UV) or visible photons [1]. Scintillators are widely used in medical imaging [2], high-energy physics, radiochemistry, security inspection [3], and nuclear radiation detection system [4]. In general, scintillators can be classified into two major categories: inorganic and organic scintillators [5]. Inorganic scintillators are available as single crystals, glasses, transparent ceramics, and typically offer high light yield but are difficult to produce in large sizes, require high-temperature processing [6] and are expensive to manufacture. Organic scintillators, which include crystalline organic materials, liquids, and plastics, provide an alternative route due to their low cost and ease of fabrication.

Organic crystals can achieve high light yield like inorganic scintillators; however, they are fragile and challenging to grow in large sizes, limiting their use for many applications. Liquid and plastic scintillators share similar compositional frameworks, typically consisting of a polymeric matrix, a primary scintillator, and an optional secondary scintillator (wavelength shifter). While both can be produced at a large scale, liquid scintillators contain toxic aromatic solvents and pose flammability risks, making them unsuitable for many applications. Plastic scintillators, by contrast, are safe, non-toxic, fast in response, versatile in devices, and easy to fabricate in various shapes at low cost [7]. For example, Bertrand reported that fabricating a plastic scintillator of 3.8 cm × 36 cm × 173 cm costs approximately USD 2000, whereas an NaI(Tl) scintillator of 5 cm × 10 cm × 41 cm costs around USD 6000 [8].

A wide range of plastic scintillators has been developed using matrices such as polystyrene (PS) [9], polymethyl methacrylate (PMMA) [10], polyvinyl toluene (PVT) [11], epoxy [12] and others. Epoxy-based scintillators offer several advantages, including high optical transparency, room-temperature curing, chemical resistance, and the ability to form complex geometries [13]. In plastic scintillators, the primary scintillators and wavelength shifters are responsible for

efficiently transferring and converting the energy deposited by ionizing radiation. High solubility in matrix is a key requirement, and the incorporation of molecules such as 2,5-diphenyloxazole (PPO) and 1,4-bis(5-phenyloxazol-2-yl)benzene (POPOP) has been demonstrated to improve solubility without compromising scintillation performance [14].

Each component in a plastic scintillator has its own role in the scintillation process. The matrix is the medium in which most interaction ionizing radiation and matter occur. When ionizing radiation passes through the plastic scintillator, it transfers energy into the matrix, exciting its molecular states. This energy transfer is efficient because the excited-state energy of the matrix is comparable to or higher than that required to excite the primary scintillator molecules. Upon relaxation to the ground state, the primary scintillator emits photons predominantly in the ultraviolet (UV) region. However, UV photons are not optimal for light transport due to strong self-absorption within the scintillator material. To minimize UV reabsorption, a secondary scintillator, commonly referred to as a wavelength shifter, is incorporated. The wavelength shifter absorbs the UV photons and re-emits them at longer wavelengths, typically in the blue or visible region. This wavelength conversion is critical because visible photons propagate more efficiently through the plastic scintillator and are better matched to the spectral sensitivity of photodetectors. A schematic illustration of the scintillation mechanism in plastic scintillator is presented in Figure 1.

Despite their numerous advantages, such as being non-toxic, cheap, and easy to produce in large size [15], plastic scintillators still face limitations, including low density, relatively low light yield, and low atomic number factor, which contribute to poor photopeak formation and limited gamma ray detection efficiency [16]. Plastic scintillators have been widely used for radiation measurement; therefore, they have attracted considerable interest from both industry and academia for further performance enhancement through chemical composition modification. One common strategy involves incorporating high-atomic-number materials to increase the scintillator density and enhance the interaction probability between ionizing radiation and the scintillator matrix, thereby improving light yield and overall detection efficiency. In general, plastic scintillators exhibit emission wavelengths in the ultraviolet (UV) to blue region, with light yields typically ranging from several thousand up to approximately 10,000 ph·MeV^{-1} [17]. Previous studies have reported that loading plastic scintillators with heavy metals can significantly improve gamma-ray detection efficiency [18]. For instance, Cherepy *et al.* demonstrated that bismuth-loaded polyvinylcarbazole (PVK) activated by the iridium complex achieved a light yield exceeding 30,000 ph·MeV^{-1}, nearly three times higher than that of undoped PVK, which exhibited a light yield of approximately 12,000 ph·MeV^{-1} [19]. In addition, perovskite-loaded plastic scintillators have been reported to reach a detection efficiency of up to 88% relative to those of commercial sintilators [12].

Although many studies have investigated plastic scintillators modified with heavy-metal loading, halide perovskites, or rare-earth dopants, most have focused on PS- or PVT-based matrices. Research on epoxy-based plastic scintillators incorporating functional oxide-type perovskites such as $LaMnO_3$ remains extremely limited. Existing literature primarily reports halide perovskites (e.g., $CsPbX_3$) or rare-earth

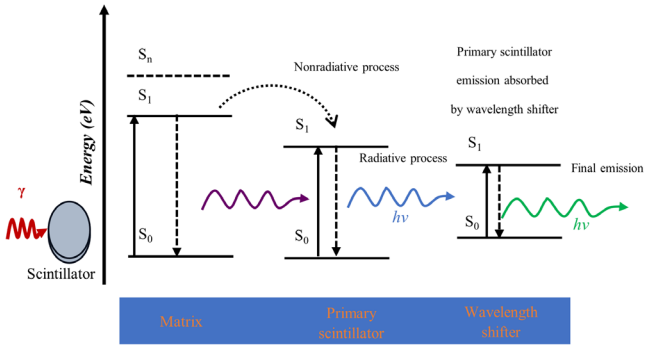

Figure 1. Scintillation mechanism of plastic scintillator.

ions such as Eu^{3+} and Ce^{3+} for enhancing optical performance, with minimal attention to oxide perovskites in polymer hosts. Furthermore, the dual emission centers of $LaMnO_3$ (Mn^{3+}/Mn^{4+}) have not been systematically evaluated for their ability to improve scintillation behavior. No prior study has simultaneously examined the structural characteristics, optical emission pathways, energy-transfer mechanisms, and radiation-detection performance of epoxy scintillators modified with $LaMnO_3$. This gap forms the central motivation for the present work.

In this context, $LaMnO_3$ represents a promising yet unexplored dopant for epoxy-based scintillators. As a perovskite oxide containing a rare-earth A-site ion (La^{3+}) and mixed-valence Mn^{3+}/Mn^{4+} centers [1], $LaMnO_3$ provides multiple radiative recombination pathways that can broaden the emission spectrum and enhance spectral matching to the sensitivity range of photomultiplier tubes (PMTs). Unlike halide perovskites, which suffer from instability and moisture sensitivity, $LaMnO_3$ exhibits high chemical and thermal stability, making it compatible with epoxy matrices. Its broadband emission and robust structure offer a new mechanism to enhance light yield and detection efficiency in plastic scintillators. Therefore, incorporating $LaMnO_3$ introduces a novel approach distinct from previous perovskite- or rare-earth-doped plastic scintillator studies.

In this study, epoxy-based plastic scintillators were fabricated using PPO as the primary scintillator, POPOP as the wavelength shifters, and $LaMnO_3$ as a dopant. $LaMnO_3$ is an oxide perovskite with the general formula ABO_3, where La^{3+} contributes multiple 4f-related energy levels enabling broad optical absorption, while Mn ions provide mixed-valence emission centers essential for visible-light generation [20,21,26]. $LaMnO_3$ powder was synthesized via the hydrothermal method [22], and the resulting scintillator composites were produced through polymerization. The combined structural, optical, and radiation-detection evaluations presented in this work aim to clarify the role of $LaMnO_3$ in improving scintillation performance and to address the identified gaps in the literature.

2. Experimental

2.1 Synthesis of $LaMnO_3$

The $LaMnO_3$ powder was synthesized by the hydrothermal method, as illustrated in Figure 2. Lanthanum nitrate hexahydrate ($La(NO_3)_3{\cdot}6H_2O$) and manganese nitrate tetrahydrate ($Mn(NO_3)_2{\cdot}4H_2O$) were used as precursors, while citric acid ($C_6H_8O_7{\cdot}H_2O$) served as a chelating agent. The molar ratio of citric acid to total metal ions (CA/M) was maintained

at 0.5. Each component was dissolved separately in distilled water, and the resulting solutions were mixed and stirred for 30 min using a magnetic stirrer. Ammonium hydroxide (NH_4OH) was then added dropwise to the mixture until the pH reached approximately 7. The final solution was transferred into a Teflon-lined stainless-steel autoclave, securely sealed, and placed in an oven for hydrothermal treatment at 180°C for 24 h. The heat treatment was performed using a controlled heating rate of 600°C·h^{-1} up to the target temperature. Furnace cooling was employed to ensure gradual temperature reduction and to minimize thermal stress, which could otherwise induce microstructural defects or secondary phase formation. After completion of the synthesis process, the samples were allowed to cool naturally inside the furnace without applying external cooling rate control. After the reaction, a white precipitate formed at the bottom of the teflon and was collected and washed several times with distilled water and ethanol. The obtained precipitate was subsequently dried at 190°C for 2 h and finally annealed at 900°C for 12 h.

2.2 Fabrication of plastic scintillator

The synthesized $LaMnO_3$ material was utilized as a dopant in the fabrication of plastic scintillators. The plastic scintillators were prepared using epoxy as the matrix, 2,5-Diphenyloxazole (PPO) as the primary scintillator, and 1,4-bis(5-phenyloxazol-2-yl) benzene (POPOP) as the wavelength shifter, with $LaMnO_3$ serving as the dopant. Based on previous studies reported by Soo Nam *et al*., the optimal concentrations of PPO and POPOP were fixed at 0.2 wt% and 0.01 wt%, respectively [20,12]. The detailed composition of each component is summarized in Table 1. The plastic scintillators were fabricated using a polymerization method, as schematically illustrated in Figure 2 .

Each component was thoroughly mixed and stirred using a magnetic stirrer at 60°C for 2 h. Afterward, the mixture was allowed to cool to room temperature before pouring into a mold. The molded mixture was then stored in a desiccator for 48 h to ensure proper curing before being carefully removed from the mold.

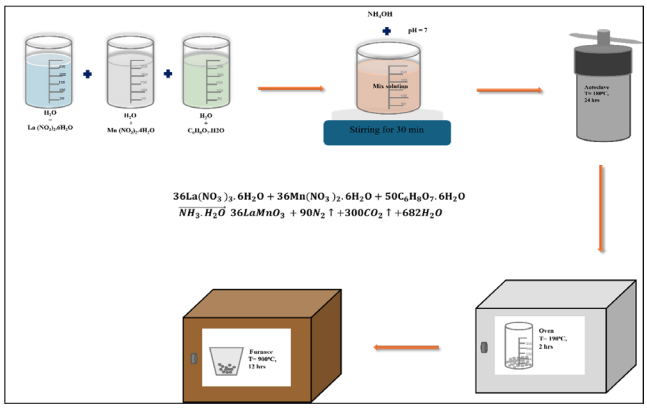

Figure 2. A sketch for the hydrothermal synthesis method of $LaMnO_3$.

Table 1. Composition of each component of the plastic scintillator.

Plastic scintillator	Epoxy [%]	PPO [%]	POPOP [%]	$LaMnO_3$ [%]
Epoxy + PPO + POPOP	>99	0.2	0.01	-
Epoxy + PPO + POPOP + $LaMnO_3$	>99	0.2	0.01	0.001

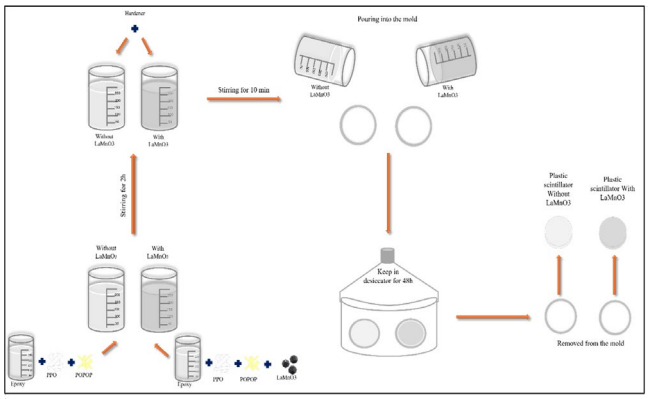

Figure 3. Illustrates a diagrammatic drawing for the polymerization method of plastic scintillator.

2.3 Characterization techniques

The morphology of the $LaMnO_3$ powders, PPO, POPOP powders, and fabricated plastic scintillators was examined using a scanning electron microscope (SEM, Quanta 650, Thermofisher Scientific). The elemental composition was analyzed by energy-dispersive spectroscopy (EDS, Xplore 15, Oxford Instruments). The crystal structure and phase composition were examined by using X-ray diffractometry (XRD, Aeris Benchtop, Malvern Panalytical) with Cu Kα radiation (λ = 1.5405 Å), and the instrument tube voltage and current were operated at 40 kV and 15 mA, respectively. XRD measurements were carried out in the 2θ range of 5° to 90° using a step size of 0.0217° and a scan rate of approximately 12.1°·min^{-1}. The surface chemical composition and oxidation states of the elements were investigated by X-ray photo-electron spectroscopy (XPS, Kratos Analytical) using Al Kα radiation. A Photoluminescence Microspectrometer (PL, Horiba Scientific) was used to record the photoluminescence spectra of each sample. Reflectance and absorption spectra of samples were recorded using UV Vis spectrophotometer (UV-Vis, Cary 100, Agilent).

3. Results and discussion

Figure 4 shows the photograph of the plastic scintillators under white light. All samples appear optically transparent. However, the undoped scintillator exhibits higher transparency compared to the $LaMnO_3$-doped scintillator.

Figure 5(a) shows the SEM image of $LaMnO_3$, which reveals irregular fine particles, consistent with the morphology reported by Dhinesh Kumar *et al*. [21]. The EDS analysis (Figure 5(b-f)) shows that the sample consists of La (61.0 wt%), Mn (21.2 wt%), and O (17.8 wt%), confirming the presence of the constituent elements of $LaMnO_3$. The La and Mn contents exhibit a near-stoichiometric ratio, indicating that the cationic composition is close to the expected La:Mn = 1:1 ratio for $LaMnO_3$.

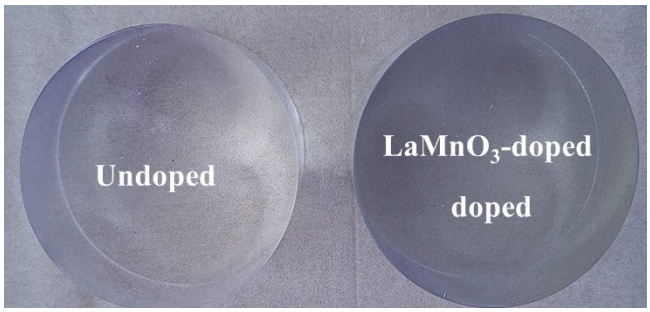

Figure 4. Photograph of undoped (left) and $LaMnO_3$-doped (right) plastic scintillators under white light.

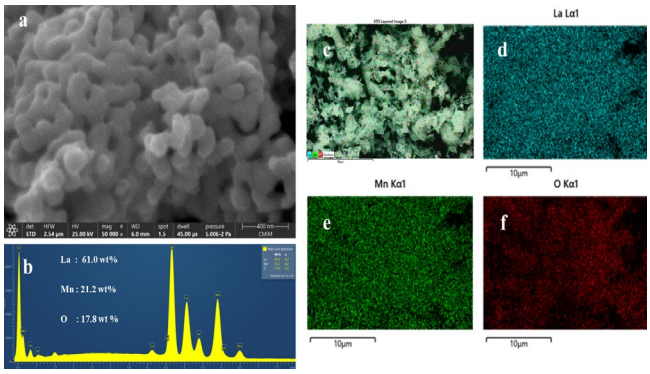

Figure 5. (a) Surface micrograph, (b) EDS spectrum with elemental percentage composition, and (c-f) elemental color mapping of various elements of $LaMnO_3$.

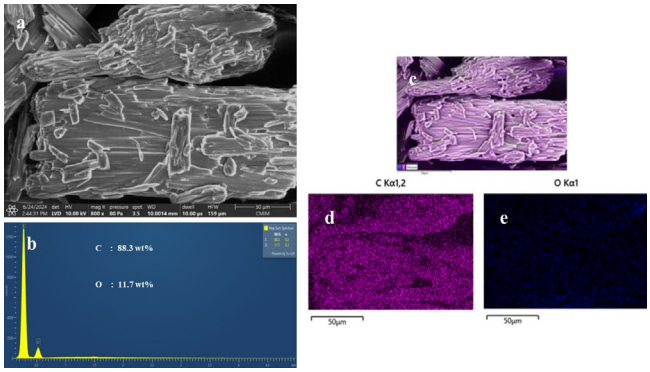

Figure 6. (a) Surface micrograph, (b) EDS spectrum with elemental percentage composition, and (c-e) elemental color mapping of various elements of PPO.

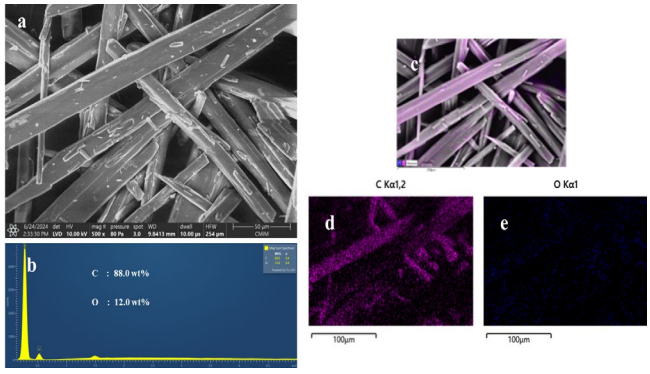

Figure 7. (a) Surface micrograph, (b) EDS spectrum with elemental percentage composition, and (c-d) elemental color mapping of various elements of POPOP.

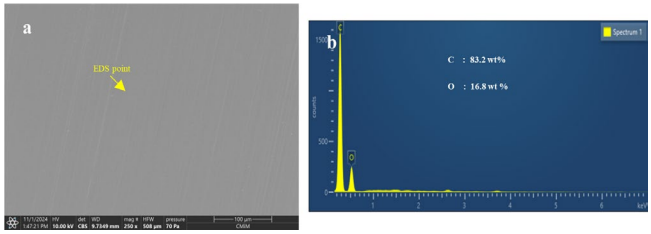

Figure 8. (a) Surface micrograph, and (b) EDS spectrum with elemental percentage composition of undoped plastic scintillator.

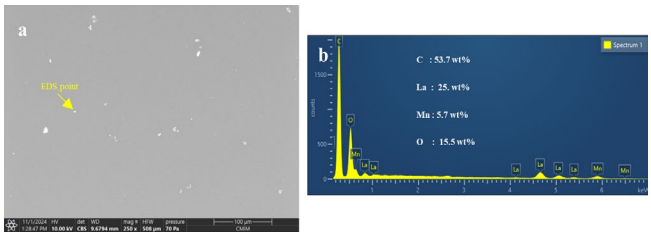

Figure 9. (a) Surface micrograph, (b) EDS spectrum with elemental percentage composition of $LaMnO_3$-doped plastic scintillator.

Importantly, no extraneous elements were detected in the EDS spectrum, and the compositional results are consistent with the XRD analysis, which confirms the formation of a single-phase $LaMnO_3$ structure (Figure 10(a)). Therefore, the EDS data supports the successful synthesis of chemically homogeneous $LaMnO_3$ without detectable impurity phases. SEM images of PPO and POPOP (Figure 6(a) and Figure 7(a)), reveal that PPO has a sheet-like morphology, while POPOP exhibits a predominantly rod-like structure. The EDS analysis confirms that both components consist of C and O, with C as the dominant element, which is consistent with their organic molecular structure.

Figure 8(a) shows SEM images of the undoped plastic scintillator, which exhibits a smooth and clean surface. In contrast, Figure 9(a) reveals the presence of fine particles on the surface of $LaMnO_3$-doped scintillator. Based on the EDS analysis, the particles detected on the doped sample contain La, Mn, O, and C. Figure 9(b) confirm the incorporation of $LaMnO_3$ within the plastic scintillator matrix.

X-ray diffraction patterns for synthesized $LaMnO_3$, PPO, and POPOP powders and the fabricated plastic scintillators were recorded to evaluate phase purity and crystal structure. The diffractograms of all components and the plastic scintillators are presented in Figure 10. Several diffraction peaks are observed for $LaMnO_3$ at approximately 22.97°, 32.66°, 40.17°, 46.67°, and 58.06°, which can be attributed to the (012), (104), (202), (024), and (214), with the most intense peak located at 32.66°, which is consistent with the report by Dhinesh *et al.*, 20218 [21]. The XRD profile of the $LaMnO_3$ matches well with the International Centre for Diffraction Data (ICDD) reference pattern for Lanthanum Manganite ($LaMnO_3$), reference code 04-024-9148. All detected diffraction peaks can be indexed to a single-phase $LaMnO_3$ with a hexagonal crystal system and space group *R-3c* [30], confirming that the $LaMnO_3$ was successfully synthesized with high phase purity. The crystallite size of $LaMnO_3$ was calculated using Scherrer Equation,

$$D = \frac{K\lambda}{\beta \cos\theta} \quad (1)$$

Table 2. Crystallographic parameters of the synthesized $LaMnO_3$.

Crystal phase	Phase fraction	a [Å]	b [Å]	C [Å]	A [Å]	B [Å]	Γ [Å]	Crystallite size [nm]	Crystal system	Space group
$LaMnO_3$	100.00	5.51	5.51	13.32	90.00	90.00	120.00	41	Hexagonal	R-3 c

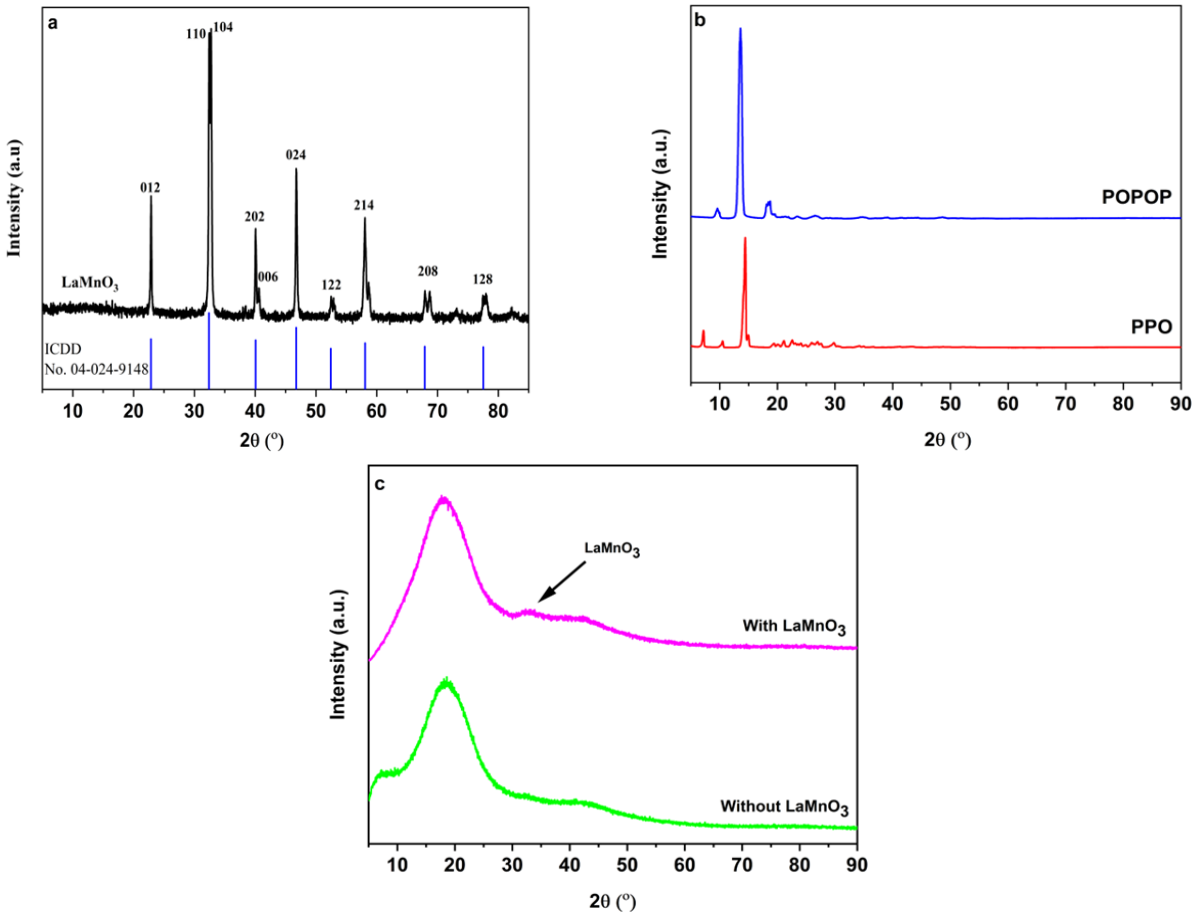

Figure 10. XRD patterns of (a) $LaMnO_3$, (b) PPO, POPOP and (c) undoped and $LaMnO_3$-doped plastic scintillator, respectively.

where D is the estimated crystallite size, K is the Scherrer constant (shape factor), λ is the X-ray wavelength (Cu Kα = 1.5418 Å), β is the full width at half maximum (FWHM), and θ is the Bragg diffraction angle. The crystallite size was estimated to be 41 nm, as shown in Table 2. In addition, a chelating agent plays a critical role in achieving phase-pure $LaMnO_3$. Based on our prior synthesis optimization, the molar ratio of citric acid to total metal ions strongly influences phase evolution and crystallinity. An appropriate citric acid–to–metal ion ratio promotes homogeneous metal–citrate complexation, leading to uniform nucleation and suppressing the formation of secondary manganese or lanthanum oxide phases. In contrast, insufficient or excessive citric acid can result in incomplete chelation, which may degrade phase purity. Additionally, the diffraction patterns of PPO and POPOP powders were compared with their corresponding reference data, and the obtained diffractograms are consistent with reference code 00-057-1713 and 00-027-1860, respectively. Figure 10(d-e) present the diffraction patterns of the fabricated plastic scintillators.

The most prominent diffraction feature for both fabricated plastic scintillators appears at $2\theta \approx 18.5°$. The broad peak at this position confirms the predominantly amorphous nature of the polymer matrix. In contrast, the presence of a weak, sharp diffraction peak at $2\theta \approx 32.69°$ in the $LaMnO_3$-doped scintillator indicates the existence of the $LaMnO_3$ phase, and its position closely corresponds to the main peak observed in the pure $LaMnO_3$ pattern as shown in Figure 10(a).

Figure 11 presents the XPS spectra of $LaMnO_3$, providing insight into the chemical composition and valence states of the constituent elements. The survey spectrum (Figure 11(a)) confirms the presence of La, Mn, and O without detectable impurity elements. The C 1s peak at 284.39 eV (Figure 11(b)) was used as a reference for binding energy calibration [21]. The O 1s spectrum (Figure 11(c)) can be deconvoluted into two components located at 529.00 eV and 530.69 eV, which are attributed to lattice oxygen associated with Mn–O bonding and oxygen related to La–O bonding, respectively. The presence of a higher binding energy O 1s component may also indicate oxygen deficiency or surface-related oxygen species. As shown in Figure 11(d), the Mn 2p spectrum exhibits two main peaks centered at 641.77 eV and 653.17 eV, corresponding to the Mn $2p_{3/2}$ and Mn $2p_{1/2}$ core levels, respectively. These binding energy values are consistent with those reported for perovskite-type $LaMnO_3$ [29]. The asymmetric peak shapes and noticeable peak broadening suggest the coexistence of Mn^{3+}

and Mn^{4+} oxidation states. Such mixed-valence behavior is commonly associated with oxygen vacancies, which play a crucial role in charge compensation and electronic structure modulation in $LaMnO_3$. The La 3d XPS spectrum (Figure 11(e)) displays characteristic spin–orbit split doublets of La $3d_{5/2}$ and La $3d_{3/2}$. The La $3d_{5/2}$ peaks are located at 833.63 eV and 837.90 eV, together with La $3d_{3/2}$ peaks at 850.42 eV and 854.68 eV, confirm the presence of La^{3+} in the perovskite lattice. Overall, the XPS results indicate that oxygen vacancies induce mixed Mn^{3+}/Mn^{4+} valence states, which are expected to contribute to the formation of multiple emission centers and play an important role in the enhanced and broadened photoluminescence behavior observed in the $LaMnO_3$-doped plastic scintillator.

The reflectance spectrum of $LaMnO_3$ is shown in Figure 12(a). The curve presents the reflectance percentage of $LaMnO_3$ as a function of the wavelength in the range of 200 nm to 800 nm. A notable decrease in reflectance is observed, from approximately 14% at 200 nm to a stable level of 6% to 8% at longer wavelengths ($\lambda > 400$ nm). This behavior indicates stronger light absorption by $LaMnO_3$ in the UV region ($\lambda > 400$ nm), where the reflectance is significantly reduced.

The reflectance data were subsequently used to estimate the optical band gap of $LaMnO_3$ using Tauc's method [22]. The calculation is represented in Equation (1-2), which correspond to Tauc's plot for $LaMnO_3$ as presented in Figure 12(b).

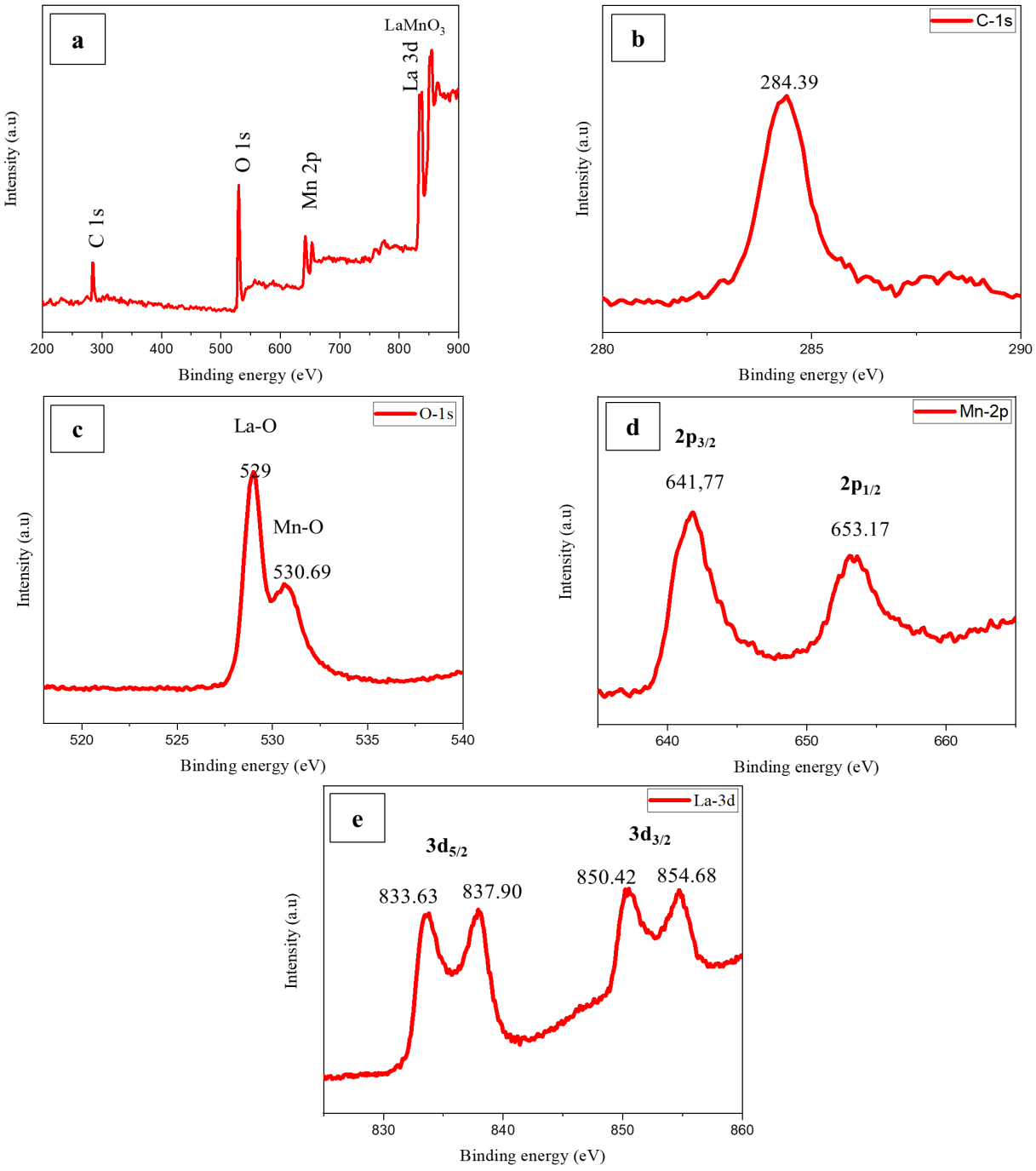

Figure 11. XPS spectra of $LaMnO_3$: (a) survey spectrum, (b) C 1s, (c) O 1s, (d) Mn 2p, and (e) La 3d.

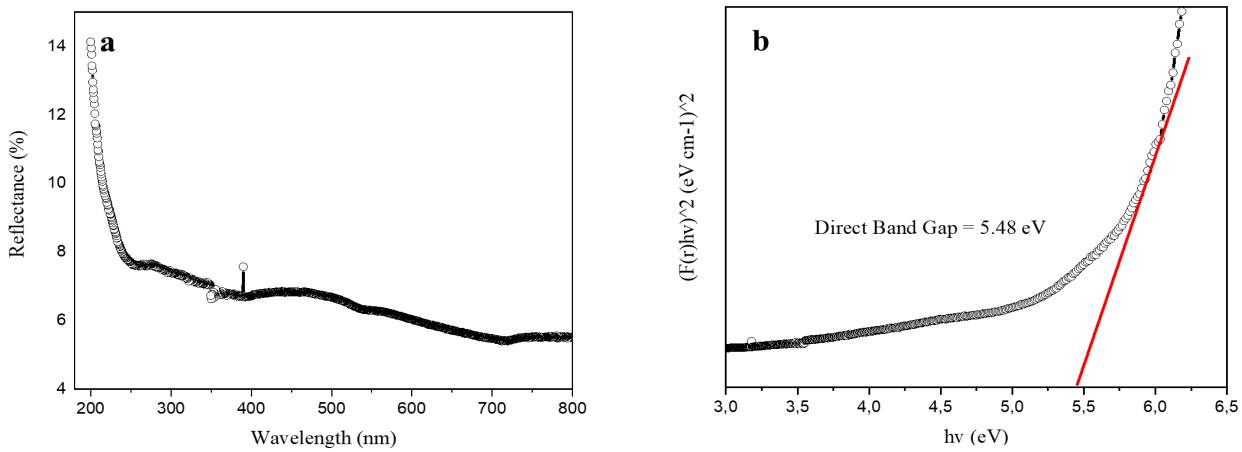

Figure 12. (a) Reflectance spectrum, and (b) the plot of $(F(R)hv)^2$ vs. photon energy (hv) of $LaMnO_3$.

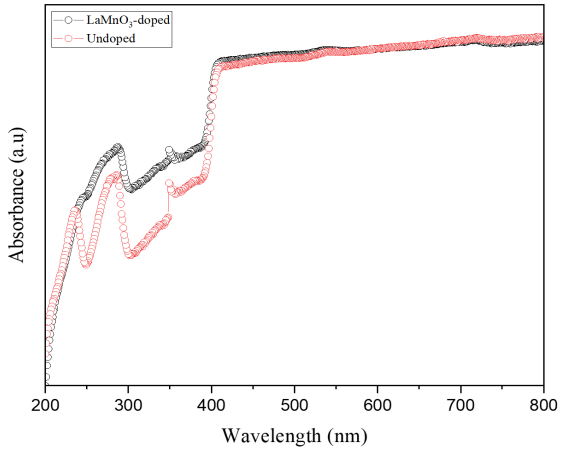

Figure 13. Absorbance spectra of fabricated scintillators.

$$[F(R)hv]^n = A(hv - E_g) \quad (2)$$

$$F(R) = \frac{(1-R)^2}{2R} \quad (3)$$

where *F(R)* is the Kubelka–Munk function, *R* is the reflectance value, *hv* is photon energy, E_g is band gap energy, *n* is a constant related to different types of electronic transitions, and *A* is an energy-independent constant. The straight red line of the curve in Figure 12(b) was extrapolated to the x-axis, indicating the direct band gap energy of $LaMnO_3$. According to the extrapolation (shown in red line), the direct band gap is approximately 5.48 eV for $LaMnO_3$. This relatively large band gap confirms that $LaMnO_3$ behaves as a wide-band-gap semiconductor, with strong absorption occurring predominantly in the UV region. This characteristic aligns with the requirements noted by Lempicki *et al.* [23]. For scintillator applications, materials with a large bandgap are essential. A small bandgap can lead to nonradiative transitions dominating the material's behavior, resulting in low luminescence. This limits the scintillator emission to levels that may fall outside the sensitivity range of the photodetector.

Figure 13 shows the absorbance spectra of the $LaMnO_3$-doped (black curve) and undoped (red curve). The undoped scintillator exhibits lower absorbance across the entire wavelength range, particularly in the UV region. In contrast, the $LaMnO_3$-doped sample shows significantly higher absorbance between 200 nm and 400 nm. Based on the band gap estimation ($E_g \approx 5.48$ eV), $LaMnO_3$ can be classified as a wide-band-gap material, corresponding to its fundamental electronic transitions. These transitions are associated with π⟶π and n⟶π excitations, which govern its optical absorption behavior [24] . The enhanced UV absorption is attributed to Mn^{3+} and Mn^{4+} charge transfer transitions within the $LaMnO_3$ lattice, providing additional excitation pathways that support radiative recombination. The result suggests that the incorporation of $LaMnO_3$ enhances the scintillator's ability to absorb high-energy radiation, including UV, X-rays, and gamma rays, which is crucial for initiating the scintillation process [25]. The higher radiation absorption increases the probability of photon generation and detection by the photodetector, potentially contributing to improved light yield.

Figure 13 shows the emission spectra of all the components used in the fabricated plastic scintillators, excited under monochromatic light at 325 nm. The emission spectra of PPO and POPOP are presented in Figure 14(a-b). PPO exhibits emission peaks at approximately 327 nm and 412 nm, whereas POPOP shows a dominant peak around 464 nm, with a significantly higher intensity than PPO. The emission spectrum of $LaMnO_3$ (Figure 14(c)) is broad, spanning 450 nm to 750 nm, although its intensity is much lower compared to PPO and POPOP. A direct comparison of the emission intensities of all components is shown in the combined spectra in Figure 14(d).

The emission spectra of $LaMnO_3$-doped and undoped scintillators are shown in Figure 15, represented by the black and red curves, respectively. The $LaMnO_3$-doped scintillator exhibits a broader emission profile with higher intensity than the undoped sample, with two distinct maxima located at approximately 399 nm and 418 nm. These emission features exhibit strong spectral overlaps with the PPO emission band and the POPOP absorption/emission region, respectively. The spectral broadening induced by $LaMnO_3$ improves wavelength matching within the PPO–POPOP system by increasing overlap and reducing dependence on precise resonance conditions. This enhanced overlap promotes more efficient energy transfer and photon conversion, thereby contributing to the increased scintillation output observed in the $LaMnO_3$-doped composite.

The higher overall intensity of the black curve indicates that $LaMnO_3$ enhances the efficiency of converting radiation energy into

visible light, resulting in improved luminescence performance of the plastic scintillator. The incorporation of $LaMnO_3$ modifies the electronic structure of the scintillator by introducing additional energy levels and broadening the distribution of existing states. As a result, the emission is distributed over a wider spectral region rather than being confined to a narrow wavelength range.

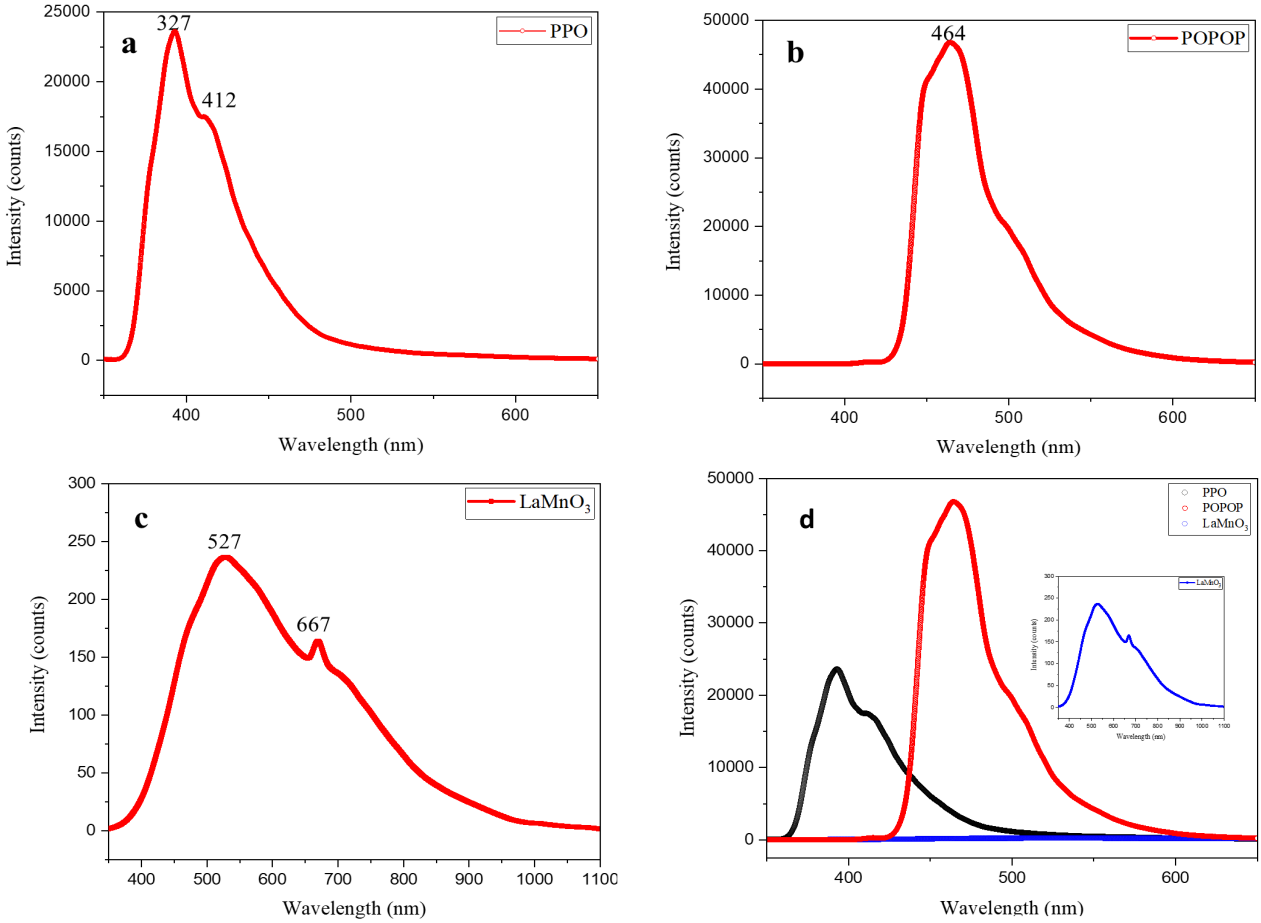

Figure 14. Emission spectra of (a) PPO, (b) POPOP, (c) $LaMnO_3$, and (d) combined emission spectra

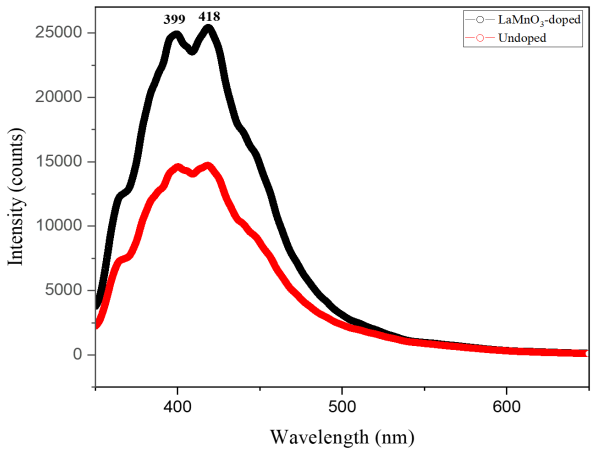

Figure 15. Emission spectra of fabricated plastic scintillators

The photoluminescence analysis is complemented by microscopic observations, including micrographs and emission mapping, as shown in Figure 16.

Figure 16(a) exhibits a uniform and smooth surface with minimal observable features, suggesting a homogeneous composition and the absence of distinct particles within the scintillator matrix. In contrast, Figure 16(b) reveals the presence of distinct particles or clusters, indicating that the incorporation of $LaMnO_3$ induces visible microstructural changes in the scintillator. These features may arise from $LaMnO_3$ particles acting as nucleation centers or from partial phase segregation within the host polymer matrix. The emission mapping image in Figure 16(c) shows relatively weak and localized luminescence, with light confined to a limited area. This observation suggests a lower density of luminescent centers and a narrower emission distribution, which is consistent with the narrower emission peaks observed in the photoluminescence spectrum (red curve) in Figure 15. Conversely, Figure 16(d) displays a significantly brighter and more spatially extended luminescence, indicating an increased number of active luminescent centers and more efficient energy emission over a larger area due to the presence of $LaMnO_3$. The enhanced blue emission observed in the emission mapping of the $LaMnO_3$-doped plastic scintillator corroborates the higher PL intensity shown by the black curve in Figure 15. In addition, interfacial interactions between $LaMnO_3$ particles and the epoxy matrix may also contribute to the observed photoluminescence enhancement. The surface of $LaMnO_3$ typically contains oxygen vacancies and mixed Mn^{3+}/Mn^{4+} states, which generate localized electronic states that can act as recombination centers or energy transfer pathways [27]. In polymer–inorganic nanocomposites,

electronic coupling and charge transfer processes at the interface can significantly modify optical absorption and photoluminescence behavior [28]. The oxygen-containing functional groups of the epoxy matrix may further promote interfacial bonding with $LaMnO_3$ surfaces, facilitating energy transfer between the polymer matrix and oxide particles. Such interfacial interactions can enhance radiative recombination efficiency, contributing to the observed increase in photoluminescence intensity and radiation detection performance.

Figure 17 compares the pulse height spectra of the plastic scintillator with and without $LaMnO_3$. Both scintillators, with dimensions of 5 cm in diameter and 2.5 cm in thickness, were optically coupled to a photomultiplier tube (PMT) and a ^{60}Co gamma source. The spectrum of $LaMnO_3$ based on the radiation spectrum, the scintillator added with $LaMnO_3$, shows a clear shift in the spectrum towards higher channels, accompanied by an increase in the overall number of counts.

Table 3. Compared the absolute detection efficiency of the plastic scintillators for the ^{60}Co gamma source.

Plastic Scintillator	N [counts]	Time [s]	Count rate [cps]	Efficiency [%]
$LaMnO_3$-doped	1181271	300	3937.6	11.59
Undoped	1005415	300	3351.4	9.86

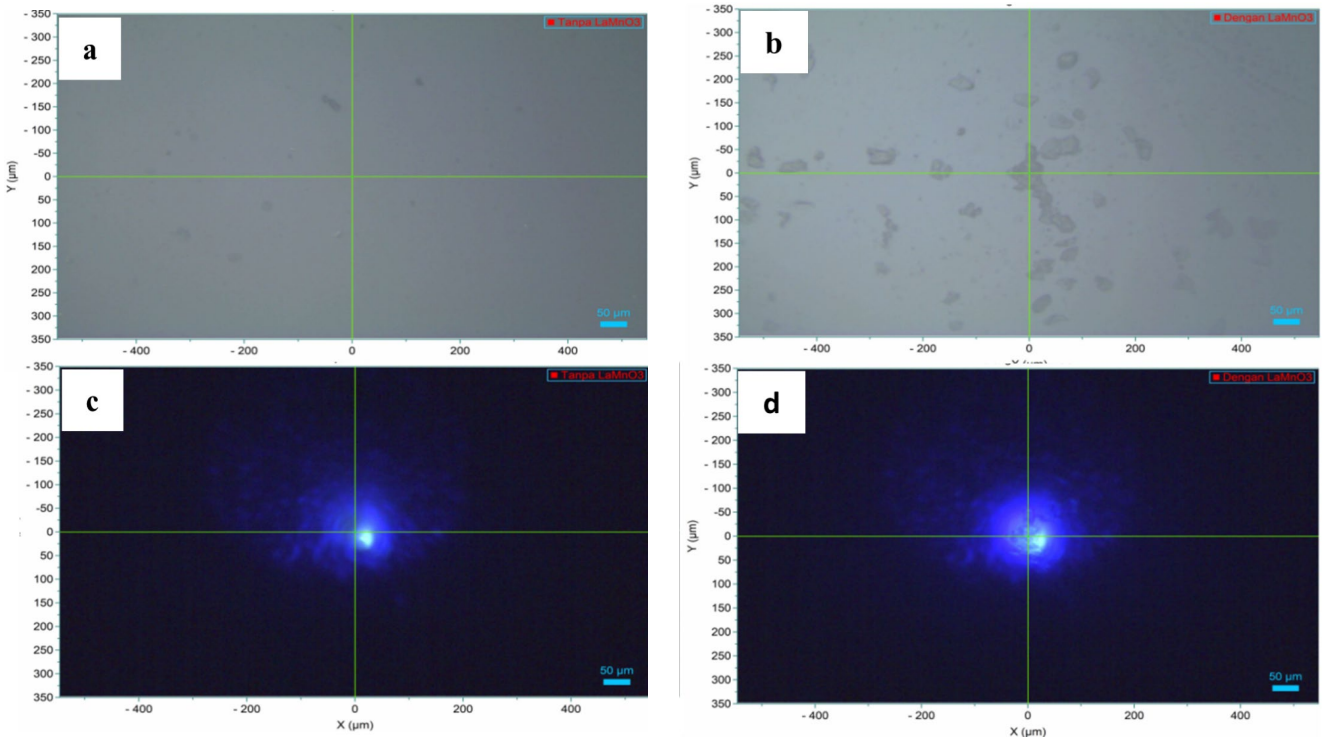

Figure 16. (a), (b) Micrograph, and (c), (d) emission mapping of fabricated plastic scintillators

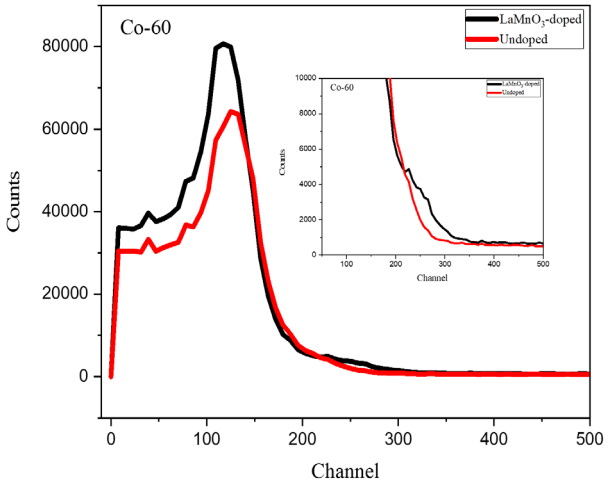

Figure 17. Pulse height spectra of fabricated plastic scintillators.

This behavior indicates that the addition of $LaMnO_3$ introduces additional radiative recombination pathways that enhance the total scintillation output. This enhancement is due to the presence of Mn^{3+} and Mn^{4+} ions, which act as multiple emission centers capable of accepting excitation energy from the epoxy as polymer host and emitting broad-band visible photons. Mn^{3+} predominantly contributes to orange-red emission, while Mn^{4+} provides deeper red emission, collectively improving its spectral overlap with the PMT sensitivity range. As a result, more optical photons are generated and detected, resulting in pulses with higher amplitudes. The observed spectral shift therefore confirms that adding $LaMnO_3$ enhances light output and improves the scintillation performance of the plastic scintillator.

Absolute detection efficiencies of plastic scintillators are calculated by Equation (4).

$$\varepsilon = \frac{N}{A.P.t} \quad (4)$$

where N is the number of detected counts, A is source activity (B_q), P is emission probability, and t is counting time. Table 3 presents the absolute detection efficiency of plastic scintillators.

The incorporation of $LaMnO_3$ into the plastic scintillator matrix resulted in a noticeable enhancement in detection efficiency compared to the undoped sample. This improvement can be attributed to the presence of $LaMnO_3$ as a high-Z inorganic additive, which increases the effective density and interaction probability between incident gamma and beta radiation and the scintillator material. Furthermore, $LaMnO_3$ introduces additional luminescent centers associated with Mn^{3+}/Mn^{4+} ions, facilitating more efficient energy transfer and photon generation within the polymer matrix. Consequently, the doped plastic scintillator exhibits higher light output, leading to an increased signal response in the photomultiplier tube and ultimately improving the overall detection efficiency.

4. Conclusions

In this work, an epoxy-based plastic scintillator doped with $LaMnO_3$ was successfully fabricated and systematically evaluated in terms of its structural, optical, and radiation-detection performance. $LaMnO_3$ synthesized via the hydrothermal method exhibited high phase purity with a hexagonal perovskite structure, near-stoichiometric La:Mn composition, and an average crystallite size of approximately 41 nm. XRD and SEM–EDS analyses confirmed the homogeneous incorporation of $LaMnO_3$ within the epoxy matrix without the formation of secondary impurity phases. XPS results revealed the coexistence of Mn^{3+} and Mn^{4+} oxidation states, originating from oxygen vacancies in the $LaMnO_3$ lattice. These mixed-valence states introduce multiple luminescent centers, which play a key role in the broadened and enhanced photoluminescence observed in the $LaMnO_3$-doped scintillator.

Optical characterization demonstrated that $LaMnO_3$ behaves as a wide-band-gap material ($E_g \approx 5.48$ eV), enabling strong absorption in the UV region. The doped scintillator exhibited significantly higher UV absorbance and enhanced PL intensity over a broader wavelength range compared to the undoped sample, indicating more efficient energy absorption and radiative recombination. Radiation response measurements using a ^{60}Co gamma source showed a clear shift of the pulse height spectrum toward higher channels and an increased total count rate for the $LaMnO_3$-doped scintillator. The absolute detection efficiency increased from 9.86% for the undoped scintillator to 11.59% for the $LaMnO_3$-doped scintillator. This enhancement is attributed to the combined effects of increased effective atomic number and density, improved radiation–matter interaction probability, and the presence of Mn^{3+}/Mn^{4+} related luminescent centers that enhance light yield and spectral matching with the PMT sensitivity.

Overall, these results demonstrate that $LaMnO_3$ is a promising and stable oxide perovskite dopant for epoxy-based plastic scintillators, offering an effective route to overcome the intrinsic limitations of conventional plastic scintillators by simultaneously enhancing optical emission characteristics and radiation-detection efficiency. From a materials-design perspective, $LaMnO_3$ was selected due to its favorable balance between structural stability, electronic properties, and compatibility with polymer-based scintillator systems. As an ABO_3-type perovskite, $LaMnO_3$ exhibits high thermal and chemical stability, which is advantageous during composite fabrication and long-term radiation exposure. The presence of Mn^{3+} ions with partially filled d orbitals enables broad emission bands via crystal-field transitions, providing good spectral compatibility with commonly used organic flours such as PPO and POPOP. Furthermore, $LaMnO_3$ does not contain heavy or toxic elements (lead-free) [31], making it a safer and more environmentally benign alternative to lead-based perovskites, while its moderate effective atomic number allows interaction with both gamma and beta radiation without inducing excessive self-absorption or optical scattering at low dopant concentrations.

Despite these advantages, $LaMnO_3$ also presents inherent limitations, including a lower intrinsic light yield compared to conventional inorganic scintillators and defect-related states associated with oxygen vacancies and mixed Mn^{3+}/Mn^{4+} valence, which may introduce non-radiative recombination pathways. Excessive particle loading may further degrade optical transparency due to increased scattering within the polymer matrix. To address these limitations, multi-dopant strategies represent a promising approach for further performance enhancement. Co-doping $LaMnO_3$ with suitable luminescent activators such as rare-earth ions (e.g., Ce^{3+}, Eu^{3+}, or Tb^{3+}) could introduce additional radiative recombination centers, improve energy-transfer efficiency, and tailor the emission spectrum to better match photomultiplier tube (PMT) or silicon photomultiplier (SiPM) sensitivity. These considerations highlight $LaMnO_3$ as a versatile perovskite platform for continued optimization of plastic scintillator performance through controlled compositional and interfacial engineering.

Conflicts of interests

The authors declare no conflict of interest.

Acknowledgements

The author would like to thank the Scholarship of National Research and Innovation Agency (BRIN), Degree by Research (DBR) Program, 2023. The author also gratefully acknowledges the full support of PT Cipta Mikro Material for this research. This study was supported by a grant from Penelitian Disertasi Doktor 2022 (No. NKB-969/UN2.RST/HKP.05.00/2022).

References

[1] A. Wibowo, Md A. K. Sheikh, L. J. Diguna, M. B. Ananda, M. A. Marsudi, A. Arramel, S. Zeng, L. J. Wong, and M. D. Birowosuto, "Development and challenges in perovskite scintillators for high-resolution imaging and timing applications," *Communications Materials*, vol. 21, 2023.

[2] L. Lu, M. Sun, Q. Lu, T. Wu, and B. Huang, "High energy X-ray radiation sensitive scintillating materials for medical imaging, cancer diagnosis and therapy," *Nano Energy*, vol. 79, p. 105437, 2021.

[3] Q. Li, D. Yang, S. Hao, R. An, R. Yuan, Y. Yang, X. Yang, M. Huang, Z. Zhang, X. Liu, and J. Zhao, "Development of the ZnO:Ga microrods - epoxy composite as a scintillation screen for ultrafast X-ray detection," *Optical Materials*, vol. 102, p. 109805, 2020.

[4] S. Jo, H. Lee, T. H. Kim, K-W. Lee, H-s. Park, H. P. Kim, and T. S. Lee, "Detecting β-radiation using a plastic scintillator containing 2,5-d iphenyloxazole-functionalized conjugated poly-fluorene," *ACS Applied Polymer Materials*, vol. 5, no. 4, pp. 2472–2480, 2023.

[5] M. Nikl, and A. Yoshikawa, "Recent R&D trends in inorganic single-crystal scintillator materials for radiation detection," *Advanced Optical Materials*, vol. 3, no. 4, pp. 463–481, 2015.

[6] N. Hayashi, and M. Koshimizu, "Development of UV-cured plastic scintillators having high scintillation light yields," *Journal of Luminescence*, vol. 277, p. 120993, 2025.

[7] Q. Chen, "Polymer composites for radiation scintillation," Ph.D. dissertation, Department of Material Science and Engineering, University of California, Los Angeles, 2012.

[8] G. Bertrand, M. Hamel, F. Sguerra, "Current status on plastic scintillators modifications," *Chemistry-A European Journal*, vol. 20, no. 48, pp. 15660–15685, 2014.

[9] N. N. Asemi, M. J. Aljaafreh, S. Prasad, S. Aldawood, and M. S. AlSalhi, "Development of a gamma-ray scintillation detector based on blue-emitting oligomers and ZnO nanoparticles," *Journal of King Saud University – Science*, vol. 34, no. 4, 2022.

[10] M. Gandini, I. Villa, M. Beratta, C. Gotti, M. Imran, F. Carulli, E. Fantuzzi, M. Sassi, M. Zaffalon, C. Brofferio, L. Manna, L. Beverina, A. Vedda, M. Fasoli, L. Gironi, and S. Brovelli, "Efficient, fast and reabsorption-free perovskite nanocrystal-based sensitized plastic scintillators," *Nature Nanotechnology*, vol. 15, no. 6, pp. 462–468, 2020.

[11] W. Li, Y. Li, and Y. Wu, "Novel organotin-loaded plastic scintillators toward gamma spectroscopy applications," *IEEE Transactions on Nuclear Science*, vol. 69, no. 9, pp. 2089–2094, 2022.

[12] H. Kang, S. Min, B. Seo, C. Roh, S. Hong, and J. H. Cheong, "Preliminary studies of perovskite-loaded plastic scintillator prototypes for radioactive strontium detection," *Chemosensors*, vol. 9, no. 3, 2021.

[13] R. M. Sahani, and A. Pandya, "Novel epoxy-bPBD-bisMSB composite plastic scintillator for alpha, beta and gamma radiation detection," *Scientific Reports*, vol. 14, no. 1, pp. 1–10, 2024.

[14] V. S. Shevelev, A. V. Ishchenko, V. V. Platonov, S. Y. Sokovnin, V. G. Il'ves, E. V. Tikhonov, O. I. Karzhenkov, and B. V. Shulgin, "Radioluminescence properties of nanocomposite scintillators with BaF 2 fillers," *Journal of Physics: Conference Series*, vol. 1115, no. 5, p. 052009, 2018.

[15] J. M. Park, H. J. Kim, Y. S. Hwang, D. H. Kim, and H. W. Park, "Scintillation properties of quantum-dot doped styrene based plastic scintillators," *Journal of Luminescence*, vol. 146, pp. 157–161, 2014.

[16] T. J. Hajagos, C. Liu, N. J. Cherepy, and Q. Pei, "High-Z sensitized plastic scintillators: A review," *Advanced Materials*, vol. 30, no. 27, 2017.

[17] H. Tsukahara, Y. Fujimoto, K. Asai, and M. Koshimizu, "Development of $LiAlO_2$ nanoparticle-loaded plastic scintillators for neutron detection," *Journal of Luminescence*, vol. 271, p. 120592, 2024.

[18] K. Rajakrishna, A. Dhanasekaran, N. Yuvaraj, K. C. Ajoy, B. Venkatraman, and M. T. Jose, "Improvement in plastic scintillator with loading of $BaFBr:Eu^{2+}$ Radioluminescence Phosphor," *IEEE Transactions on Nuclear Science*, vol. 68, no. 6, pp. 1286–1295, 2021.

[19] N. J. Cherepy, S. A. Payne, B. W. Sturm, S. P. O'Neal, Z. M. Seeley, O. B. Drury, L. K. Haselhorst, B. L. Rupert, R. D. Sanner, P. A. Thelin, S. E. Fisher, R. Hawrami, K. S. Shah, A. Burger, J. O. Ramey, and L. A. Boatner, "Performance of europium-doped strontium iodide, transparent ceramics and bismuth-loaded polymer scintillators," *Hard X-Ray, Gamma-Ray, and Neutron Detector Physics XIII*, vol. 8142, 2011.

[20] J. S. Nam, Y. S. Choi, S. B. Hong, B. K. Seo, J. K. Moon, and J. W. Choi, "Study on the characteristics of a scintillator for beta-ray detection using epoxy resin," *EPJ Web of Conferences*, vol. 153, pp. 1–6, 2017.

[21] R. D. Kumar, R. Thangappan, and R. Jayavel, "Enhanced visible light photocatalytic activity of $LaMnO_3$ nanostructures for water purification," *Research on Chemical Intermediates*, vol. 44, no. 7, pp. 4323–4337, 2018.

[22] M. S. Afify, M. M. E. Faham, U. Eldemerdash, S. I. El-Dek, and W. M. A. E. Rouby, "Effects of Ag doping on $LaMnO_3$ photocatalysts for photoelectrochemical water splitting," *Applied Physics A: Materials Science and Processing*, vol. 128, no. 10, pp. 1–12, 2022.

[23] A. Lempicki, A. J. Wojtowicz, and E. Berman, "Fundamental limits of scintillator performance," *Nuclear Instruments and Methods in Physics Research Section A*, vol. 333, no. 2–3, pp. 304–311, 1993.

[24] P. P. Nayak, B. Swain, R. R. Patro, S. S. Hota, O. P. Das, and S. Bhuyan, "Comprehensive study on the structural and optical properties of bismuth manganese oxide composite ceramic for optoelectronic applications," vol. 35, no. 4, pp. 1–8, 2025.

[25] F. Maddalena, L. Tjahjana, A. Xie, Arramel, S. Zeng, H. Wang, P. Coquet, W. Drozdowski, C. Dujardin, C. Dang, and M. D. Birowosuto, "Inorganic, organic, and perovskite halides with nanotechnology for high-light yield x- and γ-ray scintillators," *Crystals (Basel).*, vol. 9, no. 2, p. 9020088, 2019.

[26] J. M. Gallmetzer, F. R. S. Purtscher, J. Gamper, A. Mohammadi, R. Feyerherm, W. Riedel, S. Penner, and T. S. Hofer, "Combined experimental and theoretical approach to the electronic and magnetic properties of Cu-doped $LaMnO_3$ perovskites," *Journal of Physical Chemistry C*, vol. 129, no. 1, pp. 677–688, 2024.

[27] Z. Elseddig, H. Xu, D. Wang, W. Zhang, X. Guo, Y. Zhang, Z. Sun, and J. Chen, "Modulating Mn^{4+} ions and oxygen vacancies in nonstoichiometric $LaMnO_3$ perovskite by a facile sol-gel method as high-performance supercapacitor electrodes," *Electrochimica acta*, vol. 253, pp. 422–429, 2017.

[28] T. B. Atisme, Y-F. Luo, E. N. Tseng, Y-C. Chen, Y-C. Hsu, and S-Y. Chen, "Interface interactions in conjugated polymer composite with metal oxide nanoparticles," *Nanomaterials*, vol. 9, no. 11, p. 1534, 2019.

[29] D. Çoban Özkan, A. Türk, and E. Celik, "Synthesis and characterizations of $LaMnO_3$ perovskite powders using sol–gel method," *Journal of Materials Science: Materials in Electronics*, vol. 32, no. 11, pp. 15544–15562, 2021.

[30] M. De, S. Hajra, R. Tiwari, S. Sahoo, and R. N. P. Choudhary, "Structural, dielectric and electrical characteristics of $BiFeO_3$-

$NaNbO_3$ solid solutions," *Ceramics International*, vol. 44, no. 10, pp. 11792–11797, 2018.

[31] P. G. R. Achary, "Structural and electrical properties of 0.98 $(K_{0.5}Na_{0.5}NbO_3)$-0.02$(Bi_{0.5}Na_{0.5})TiO_3$ ceramics," *Journal of Metals, Materials and Minerals*, vol. 33, no. 4, pp. 1–6, 2023.